ACS Catalysis

pubs.acs.org/acscatalysis

Research Article

Operando Structure–Activity–Stability Relationship of Iridium Oxides during the Oxygen Evolution Reaction

Rik V. Mom,* Lorenz J. Falling, Olga Kasian, Gerardo Algara-Siller, Detre Teschner, Robert H. Crabtree, Axel Knop-Gericke, Karl J. J. Mayrhofer, Juan-Jesús Velasco-Vélez, and Travis E. Jones

Cite This: *ACS Catal.* 2022, 12, 5174–5184

Read Online

ACCESS | Metrics & More | Article Recommendations | Supporting Information

ABSTRACT: Creating active and stable electrodes is an essential step toward efficient and durable electrolyzers. To achieve this goal, understanding what aspects of the electrode structure dictate activity and catalyst dissolution is key. Here, we investigate these aspects by studying trends in the activity, stability, and *operando* structure of iridium oxides during the oxygen evolution reaction. Using *operando* X-ray photoelectron and X-ray absorption spectroscopy, we determined the near-surface structure of oxides ranging from amorphous to crystalline during the reaction. We show that applying oxygen evolution potentials universally yields deprotonated μ_2-O moieties and a μ_1-O/μ_1-OH mixture, with universal deprotonation energetics but in different amounts. This quantitative difference mainly results from variations in deprotonation depth: surface deprotonation for crystalline IrO_2 versus near-surface deprotonation for semicrystalline and amorphous IrO_x. We argue that both surface deprotonation and subsurface deprotonation modify the barrier for the oxygen evolution and Ir dissolution reactions, thus playing an important role in catalyst performance.

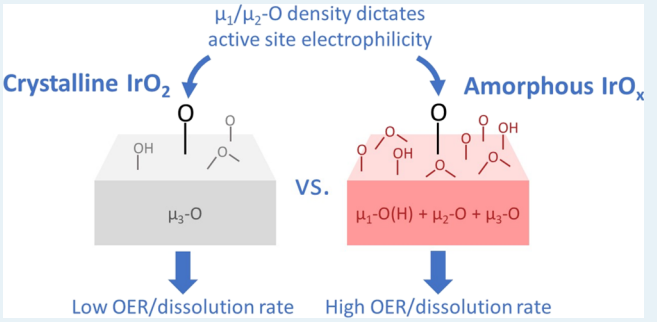

KEYWORDS: *oxygen evolution reaction, iridium oxide, X-ray absorption spectroscopy, operando spectroscopy, electrolysis, electrocatalysis*

INTRODUCTION

The production of hydrogen through water electrolysis is one of the cornerstones in sustainable chemistry, providing a storage medium for intermittent solar and wind power and a vital building block for the production of chemicals. Since the invention of electrolysis in 1789,[1,2] noble metal-based electrodes remain the state-of-the-art in acid electrolysis. For the oxygen evolution reaction (OER) side of the process, only iridium oxide offers the combination of high catalytic activity and decent stability. Unfortunately, iridium is one of the scarcest elements on Earth.[3] Hence, to enable large-scale implementation, it either needs to be used at low loading or it should be replaced.

To guide the search for improved acid OER catalysts, the question that arises is what properties determine their activity and stability. From the wide range of oxides that have been investigated, it is clear that the elemental composition of the electrode plays an important role.[4−6] The crystal structure of the oxides also has a big impact, with hydrous/amorphous oxides being reported as more active but less stable than their crystalline counterparts.[4,5,7−9] What remains unclear is through what mechanism these properties influence the oxygen evolution and electrode dissolution reactions. However, it has been established that catalyst dissolution accelerates at the OER onset potential,[4,5,8] suggesting that the two reactions share one or more intermediates. Hence, knowledge of the species present on OER catalysts under reaction conditions is essential in understanding the origins of both activity and stability.

A wide range of *operando* methods have been employed to reveal the (electronic) structure of electrodes and their dynamics under acid OER conditions, such as X-ray-based techniques,[10−18] isotope labeling,[8,19−23] and Raman spectroscopy.[12,21,24,25] They revealed that noble-metal electrodes are oxidized and deprotonated at OER potentials.[10−17,21,25−28] This oxidation is essential for creating an electrophilic character in the oxygen atoms on the surface, making them reactive for O−O coupling with water.[26,27] Indeed, it was shown that as the surface of IrO_2(110) is increasingly oxidized, the barrier for the OER is lowered.[26] During the oxidation process, there is a clear change in the Ir-oxidation state.[10,12,13,15,26−28] However, the oxidation need not only be centered on the cations. For example, the oxidative

Received: December 24, 2021
Revised: March 8, 2022
Published: April 15, 2022

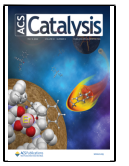

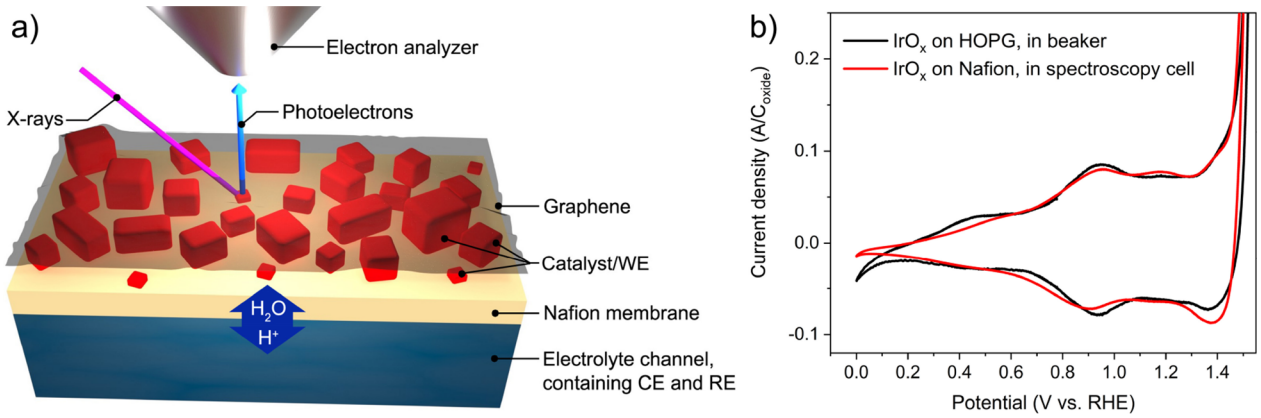

Figure 1. (a) Schematic representation of the confined electrolyte approach[10,17,29] (details in the Method section and Supporting Information section S1). (b) Comparison of the cyclic voltammogram of electrochemically oxidized Ir particles in the spectroscopy cell and in a beaker. Recorded in 0.1 M H_2SO_4 at 50 mV/s. The current density was calculated by normalization of the current to the integrated charge between 0.7 V_{RHE} and 1.4 V_{RHE}.

deprotonation of μ_2-OH groups on amorphous IrO_x is at least partially oxygen-centered,[10,11] directly aiding in creating the electrophilic character needed for the OER.

While some of the key ingredients for the OER have thus been identified, they have yet to be linked to the observed trends in activity and stability. To establish this link, it is essential to investigate trends in the surface structure of OER catalysts under reaction conditions. However, the challenges in *operando* characterization have so far largely prevented such systematic studies. Using our recently developed confined electrolyte approach for in situ X-ray photoelectron spectroscopy (XPS) and X-ray absorption spectroscopy (XAS)[10,17,29] (see Figure 1a), we are now able to thoroughly characterize a range of catalysts in an acceptable time frame. With this methodology, we unravel the *operando* structure−activity−stability relationship for iridium oxides ranging from highly hydrated, amorphous, to crystalline structures. We use O K-edge and Ir 4f spectra of a series of well-defined oxide films to obtain a quantitative comparison of the oxygen and Ir species in the oxides, allowing us to establish which structural features are universal and which correlate with activity and stability. Based on this comparison, we put forward a model in which both surface and subsurface deprotonation play a central role in determining the barrier for the OER and Ir dissolution.

METHODS

Spectroscopy. The *operando* XAS and XPS measurements were performed at the ISISS beamline at BESSY II synchrotron, Berlin, Germany, using the confined electrolyte approach recently developed by our group.[10,17,29] As depicted in Figure 1a, the catalyst layer is sandwiched between a Nafion 117 proton exchange membrane and a graphene layer. The backside of the membrane is in contact with an electrolyte flow channel, which houses the saturated Ag/AgCl reference electrode and Pt wire counter electrode. While the Nafion membrane enables water and proton transport to and from the working electrode, the graphene layer minimizes the evaporation into the near-ambient pressure XPS chamber. We have recently shown that this leads to the formation of a thin film of a liquid electrolyte around the working electrode, enabling XPS and XAS measurements under *operando* conditions.[10,17] More details on the cell geometry and beamline can be found in section S1 of the Supporting Information. To prevent beam damage effects,[17,29] each spectrum was recorded on a fresh spot on the sample and measurement times were minimized. The appropriate measurement time was established by comparing consecutive scans to find beam-induced effects, such as the reduction of μ_1-O and μ_2-O groups. In order to obtain good-quality spectra even with the minimized measurement time, which is particularly challenging for XPS, measurements from multiple spots and/or samples were averaged.

The electrochemical performance of the spectroscopy cell is demonstrated in Figure 1b. The cyclic voltammogram of electrochemically oxidized Ir recorded in the spectroscopy cell is compared to that of electrochemically oxidized IrO_x on highly oriented pyrolytic graphite in a beaker of 0.1 M H_2SO_4. Clearly, the position and relative proportion of the CV features are reproduced in the spectroscopy cell, confirming its realistic performance. With a solution resistance of 40−70 Ω, ohmic losses are modest even well in the OER regime (currents of up to 1 mA at 1.65 V_{RHE}). Note that all potentials were converted from the Ag/AgCl scale to the reversible hydrogen electrode (RHE) scale without ohmic drop correction.

Dissolution Measurements. The concentration of ^{193}Ir dissolved in 0.1 M argon-purged H_2SO_4 during the OER was measured online in an electrochemical scanning flow cell (SFC) directly coupled to an inductively coupled plasma mass spectrometer (Perkin Elmer NexION 300X spectrometer).[30] A carbon rod placed in the electrolyte inlet channel of the cell was used as the counter electrode. Saturated Ag/AgCl placed in the electrolyte outlet channel served as the reference electrode. The inductively coupled plasma mass spectrometry (ICP−MS) signal of Ir was normalized by the intensity of the ^{187}Re isotope, which was added to the solution as an internal standard downstream of the SFC. Calibration of the ICP−MS response was performed on each day of measurement. Normalization of the measured currents and dissolution rates was performed using the geometric contact area of the working electrode, which was 1 mm^2.

Sample Preparation. The semicrystalline and crystalline iridium oxide layers for spectroscopy and transmission electron microscopy (TEM) were prepared by sputter deposition of roughly 2 nm metallic Ir onto Na_2SO_4 crystals and subsequent calcination in air at 400 °C for 2 h (semicrystalline IrO_x) or 550 °C for 3 h (crystalline IrO_2). After cooling, the oxide layers

https://doi.org/10.1021/acscatal.1c05951
ACS Catal. 2022, 12, 5174−5184

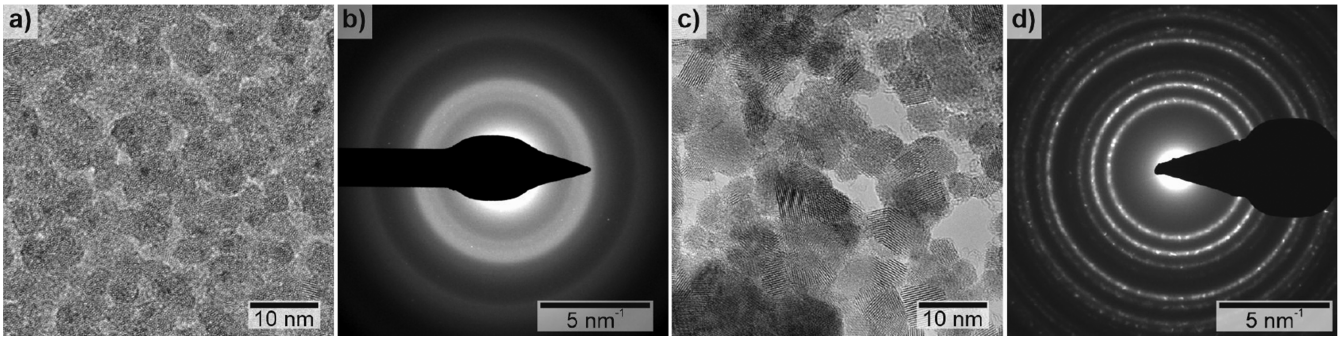

Figure 2. TEM characterization of IrO_x films transferred onto Quantifoil grids. (a,b) Semicrystalline film calcined at 400 °C for 2 h. (c,d) Crystalline (rutile) film calcined at 550 °C for 3 h.

were covered with a formvar stabilization layer and the Na_2SO_4 substrates were dissolved in ultrapure water, leaving the catalyst/formvar layers floating on the surface. The catalyst layers were scooped onto Nafion substrates for spectroscopy or onto Quantifoil grids for TEM measurements. After drying, formvar was removed using baths of chloroform, acetone, ethanol, and water. In the final step, the catalyst layer was covered with graphene. This method yields the highly homogeneous samples needed for the XPS and XAS measurements. More details can be found in Supporting Information sections S2 and S3.

To create an electrochemically oxidized IrO_x sample, Ir was sputtered directly onto Nafion. Subsequently, the samples were covered with graphene, either with or without an oxidation treatment in 3% H_2O_2 prior to applying the graphene layer. The sample was (further) oxidized in situ in the spectroscopy cell at 1.55 V_{RHE} for 2 h, followed by 30 CV's between 0 V_{RHE} and 1.55 V_{RHE}.

For dissolution measurements, a pinhole-free catalyst layer is necessary. Therefore, the working electrodes were prepared using a more gentle sputtering procedure. To create a film with low roughness, the Si/SiO_2 wafer substrate was first coated with a 10 nm Ti adhesion layer using e-beam evaporation of a Ti source (EvoChem, 99.999%). Subsequently, a 100 nm Ir film was deposited by magneton sputtering of a 3 in. Ir target (EvoChem, 99.999%) in Ar plasma, applying 100 W at 5×10^{-3} mbar. The base vacuum before sputtering was 2×10^{-8} mbar. The wafer was diced and subjected to the same oxidation treatments as the spectroscopy samples.

DFT Calculations. In order to interpret the experimental O K-edge spectra, we made use of the extensive set of simulated O K-edge spectra that was generated by our group for oxygen species on rutile IrO_2 surfaces[31] and extended them to include bulk anatase and hollandite IrO_2. We employed the Quantum ESPRESSO package version 6.1.[32] Ground-state calculations were performed using the PBE functional[33] with projector-augmented wave datasets taken from the PS Library[34] and a kinetic energy (charge density) cutoff of 30 Ry (300 Ry). The surface models contained at least five layers of IrO_2, of which all except the central two layers were allowed to relax. A k-point mesh equivalent to at least (8×8) for the (1×1) (001) rutile surface unit cell was used in conjunction with cold smearing[35] (smearing parameter 0.02 Ry). To compute the O K-edge spectra, we used a one-electron Fermi's golden-rule expression implemented in XSpectra.[36,37] We employed the same *k*-point mesh as that used for the ground-state calculations and did not make use of a core hole potential. ΔSCF calculations were used to determine the relative edge positions.[38] Subsequently, the absolute excitation energy scale of the computed spectra was set using the white-line energy of bulk rutile IrO_2, which is located at 530.0 eV. The calculations on the anatase and hollandite structures were performed on a bulk unit cell. To generate μ_2-O species within this unit cell, an Ir vacancy was introduced.

For the $IrO_2(110)$ surface, we also assessed the energetics of various levels of surface protonation using the same approach as described above. However, in this case, a 1×2 super cell was used to include coverage effects. From the total energies obtained in the DFT calculations, a free-energy diagram was constructed by applying thermodynamic corrections to the DFT reaction energies to account for the applied potential and pH (computational hydrogen electrode approach). For the molecular dynamics (MD) data in Figure 6, we made use of previous MD simulations.[26]

RESULTS

To create a series of iridium oxides with a different degree of crystallinity, we subjected metallic Ir films to three oxidation treatments: electrochemical oxidation, calcination at 400 °C, and calcination at 550 °C (see the Methods section for details). Electrochemical oxidation is known to result in an amorphous, highly hydrated oxide.[10,39−41] Indeed, the cyclic voltammogram of the electrochemically oxidized sample in Figure 1b reproduces the features reported in the literature for hydrous iridium oxide.[8,39] Calcination at 400 °C results in an intermediate level of order, as indicated by the diffuse rings in the electron diffraction pattern in Figure 2b. Further analysis (Figure 2a and Supporting Information section S3) indicates that a closed film is formed, consisting of small crystallites in a rather amorphous embedding. Full (rutile) crystallinity is reached for the sample calcined at 550 °C, as shown by its sharp diffraction pattern in Figure 2d. The film contains larger grains (Figure 2c) than its semicrystalline counterpart produced at 400 °C. However, the surface-to-bulk ratio remains similar because the sintering and growth of the crystallites opens up holes in the film, creating a porous structure. All three types of films are ultrathin, consisting of a single layer of nanometric grains. This well-defined film structure is important as it enables a quantitative comparison of the spectroscopic data of the different structures. In addition, the small grain size and excellent accessibility for the electrolyte closely recreate the conditions in the Ir black or IrO_2-based membrane-electrode-assemblies used in industrial applications.[42] Further sample characterization can be found in Supporting Information section S3.

https://doi.org/10.1021/acscatal.1c05951
ACS Catal. 2022, 12, 5174−5184

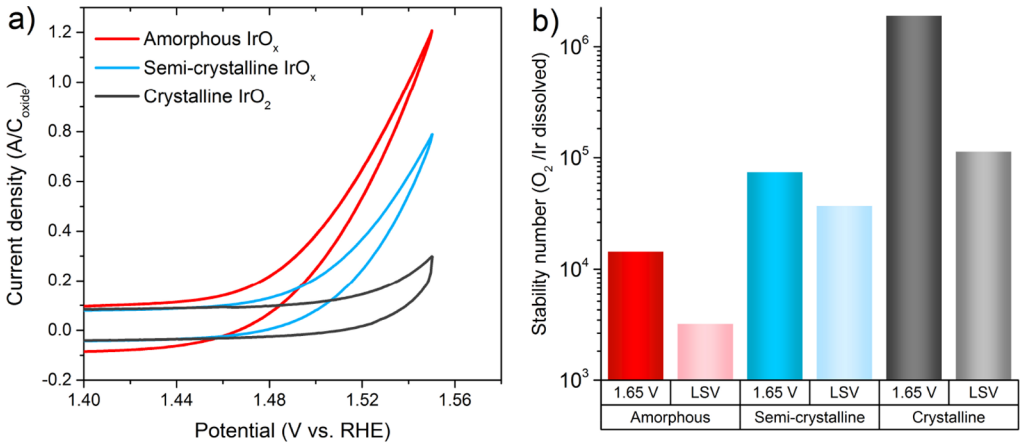

Figure 3. Activity and stability of iridium oxides. (a) Cyclic voltammograms of graphene-covered IrO_x films on Nafion, measured in the spectroscopy chamber at 50 mV/s with 0.1 M H_2SO_4. (b) Stability numbers (O_2 molecules generated per dissolved Ir atom) for IrO_x films on Si in 0.1 M H_2SO_4, calculated from the potential holding data at 1.65 V_{RHE} and LSV from 1.2 V_{RHE} to 5 mA/cm^2 at 10 mV/s (see Supporting Information section S4).

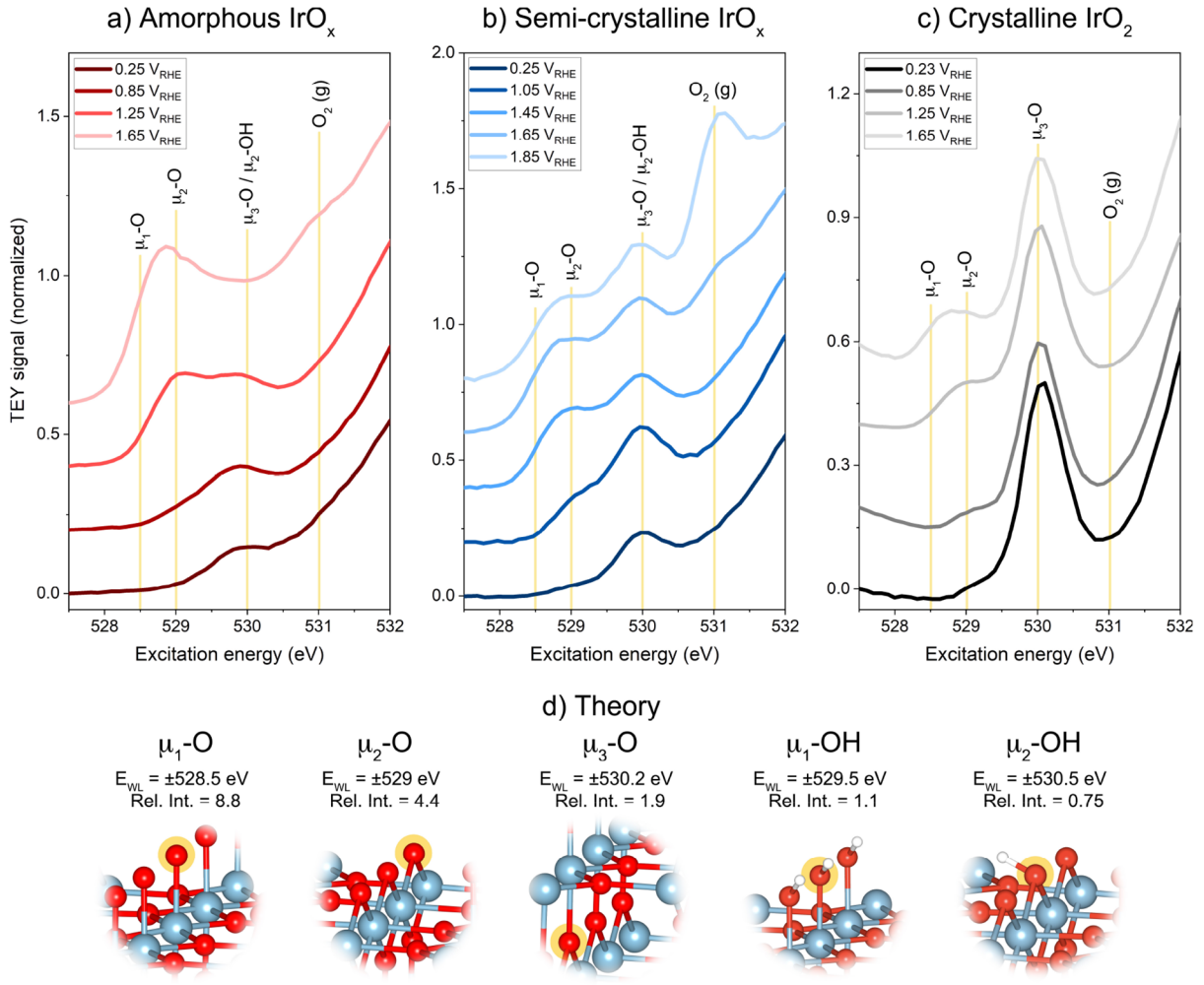

Figure 4. In situ O K-edge spectra of graphene-covered IrO_x films on Nafion during stepwise anodization. (a–c) Experimental spectra of amorphous, semicrystalline, and crystalline films, respectively, normalized to the edge jump at 550 eV. The spectra were recorded in 0.1 M H_2SO_4 using the total electron yield (TEY) detection mode, which has a probing depth of ~5 nm (see Supporting Information section S5). The main contributing O(H) species in the spectra are indicated. (d) Theoretical analysis based on O K-edge simulations for various rutile IrO_2 surface structures (see Supporting Information section S6 for details). E_{WL} denotes the white-line energy (first peak in the spectrum), and Rel. Int. designates the relative peak intensity of the white line, again normalized to the edge jump.

https://doi.org/10.1021/acscatal.1c05951
ACS Catal. 2022, 12, 5174−5184

The activity and stability of the amorphous, semicrystalline, and crystalline oxide were investigated using cyclic voltammetry and ICP−MS. In agreement with the literature,[4,5,8,9] the OER activity of the samples decreases with increasing degree of crystallinity, as shown by the cyclic voltammograms recorded in the X-ray spectroscopy setup (Figure 3a, see Supporting Information Figure S10 for ex situ measurements). The stability of the samples was studied by quantifying the dissolved Ir concentration during linear sweep voltammetry (LSV) (10 mV/s) and potential holding at 1.65 V_{RHE} (see Supporting Information Figure S11). In the former, one is predominantly sensitive to transient dissolution, which is less important in the latter. Based on these measurements, stability numbers[8] (O_2 molecules generated per dissolved Ir atom) were calculated for the amorphous, semicrystalline, and crystalline oxide. As shown in Figure 3b, the stability of the samples follows the opposite trend as the activity: the stability number increases with increasing degree of crystallinity. This trend is observed both for the predominantly transient dissolution during the linear potential sweep and during potential holding at 1.65 V_{RHE}.

To explain the activity and stability trends, we will now analyze the near-surface structure and energetics of the iridium oxides under electrochemical conditions. In particular, we will determine which aspects are similar and which show a trend that correlates with the activity/stability. First, we will describe the oxygen and iridium species that are formed when the potential is increased up to the OER range. To probe the oxygen species in IrO_x electrodes at anodic potentials, we recorded in situ O K-edge XAS spectra (Figure 4). The white-line resonances (peaks) in the range of 528−531 eV allow for a detailed speciation of the near-surface O(H) species.[10,31] For peak assignments, we use the extensive set of theoretical O K-edge spectra calculated by our group for surface species on rutile IrO_2[31] (Figure 4d and Supporting Information section S6). The various oxygen species are designated using the μ-notation here, which is more unambiguous than the CUS/bridge/bulk O(H) notation that is also commonly used. For clarity, μ_1-O corresponds to the coordinatively unsaturated site (CUS) O, μ_2-O to bridge O, and μ_3-O is associated with bulk O (but can exist at the surface as well). The universality of the O K-edge peak assignments for Ir oxides with different crystal structures was confirmed by calculations on anatase and hollandite structures (see Supporting Information Figure S14) and experimental spectra of reference compounds (see Supporting Information Figure S16).

In general, the theoretical analysis shows that OH species have a very low resonance intensity per atom. Hence, the weak shoulder observed for amorphous IrO_x at 0.25 V_{RHE} indicates that the sample is strongly hydroxylated at low potentials. In contrast, crystalline IrO_2 shows a strong contribution of μ_3-O at 530 eV, which is the only oxygen species in the bulk of rutile IrO_2.[43] The semicrystalline sample also shows a clear μ_3-O peak but with a lower intensity, consistent with the intermediate level of connectivity in the film.

Increasing the electrode potential results in the rise of a new peak at roughly 529 eV for all samples, which we assign to the formation of μ_2-O species during the oxidative deprotonation of the IrO_x films (reaction 1).

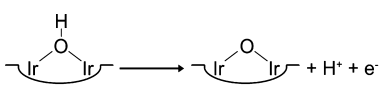

(1)

Note that the formation of μ_1-OH (reaction 2) could also have a small contribution to the peak rise.

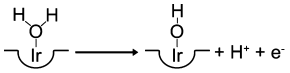

(2)

However, the relative peak intensity of μ_1-OH species is significantly smaller than that of μ_2-O, and the peak is typically found at a higher excitation energy (~529.5 eV). As a result, we expect that μ_1-OH formation is hardly visible in the O K-edge spectra. This does not mean that reaction 2 does not occur. In fact, the cyclic voltammograms in Figures 1 and S9 show surface redox currents well before the 529 eV peak starts to rise at ~0.85 V_{RHE}, suggesting that a process invisible to O K-edge spectroscopy occurs in this potential window. In agreement with this, our DFT calculations suggest that reaction 2 occurs at ~0.5 V_{RHE} (see Supporting Information section S8).

Starting at about 1.25 V_{RHE}, a broadening of the 529 eV peak toward lower excitation energy is observed, again universally for all samples. This broadening results from the rise of a peak at roughly 528.5 eV, which originates from μ_1-O species that are formed through the deprotonation of μ_1-OH (reaction 3).[10]

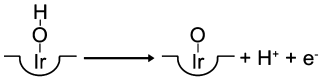

(3)

Note that reactions 1−3 are reversible, bringing the Ir oxides back to a protonated state when the potential is lowered (see Supporting Information Figure S19). More generally, the O K-edge spectra show no indication of irreversible changes in the oxide structure. For the amorphous oxide, one could imagine a thickening of the oxide shell to occur under OER conditions. However, no sign of further thickening of the oxide is observed after the initial oxidation treatment. For the semicrystalline and crystalline oxides, we also observe fully reversible behavior. Amorphization of the oxide, which is a common phenomenon for OER electrodes,[44−47] would result in a loss of μ_3-O. Figures 4 and S19 show that this is not the case here, consistent with the relatively high stability of Ir oxide electrodes.

Complementing the analysis of the oxygen species, we analyzed the Ir-oxidation states present in the samples using Ir 4f XPS spectra (Figure 5). Again, we observe that the differences in sample preparation are clearly reflected in the Ir 4f spectra of the catalysts. The spectra can be interpreted using Figure 5d, which shows that Ir^0 can be identified based on its peak position, whereas Ir^{3+} and Ir^{4+} can only be distinguished based on their Ir 4f peak asymmetry due to final-state effects.[43,48,49] Comparing the reference spectra in Figure 5d to those in Figure 5a, we see that the Ir 4f doublet of amorphous IrO_x is broad and lies between Ir^0 and $Ir^{3+/4+}$. This implies that the electrochemical oxidation procedure did not fully oxidize the sample. Rather, it contains a mixture of oxidation states, likely in the form of an oxide shell and a metallic core. In contrast, the semicrystalline IrO_x is deeply oxidized (Ir $4f_{7/2}$ at 61.8 eV), with only a small shoulder at 61 eV, hinting at some Ir^0 remnants. At 0.25 V_{RHE}, a rather symmetric doublet is observed (Figure 5b), which is typical for Ir oxides with a large fraction of Ir^{3+}[10,27,49,50] (compare to Figure 5d). For the crystalline IrO_2, an Ir^{4+} oxidation state is expected in the bulk and an Ir^{3+}/Ir^{4+} mix at the surface at low potentials. Indeed, we

https://doi.org/10.1021/acscatal.1c05951
ACS Catal. 2022, 12, 5174−5184

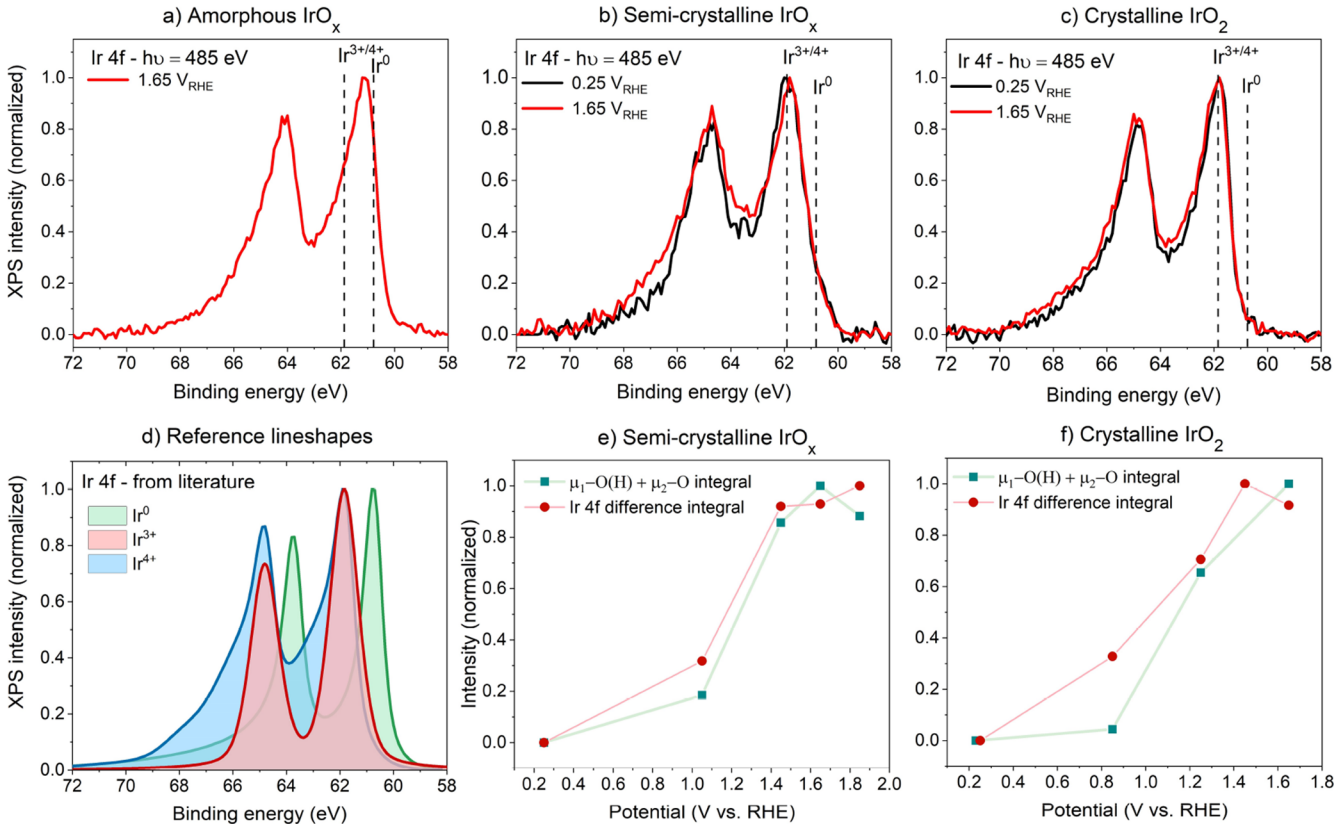

Figure 5. In situ Ir 4f XPS analysis of graphene-covered IrO_x films on Nafion during stepwise anodization. Electrolyte: 0.1 M H_2SO_4. The spectra were (Shirley) background-subtracted and normalized to the Ir $4f_{7/2}$ peak. The μ_1-O + μ_2-O signal was obtained by integration of the O K-edge spectra between 528 and 529 eV, following background subtraction and normalization to the μ_3-O intensity at 530 eV. The reference line shapes were derived from fits used in the literature for metallic Ir (Ir^0),[43] IrOOH nanosheets (Ir^{3+}),[49] and rutile IrO_2 (Ir^{4+}),[43] see Supporting Information section S10 for more details. The Ir 4f difference integrals were calculated from the difference in peak-normalized, background-subtracted spectra.

observe the asymmetric Ir 4f doublet (Ir $4f_{7/2}$ at 61.8 eV) also reported in the literature for conducting Ir^{4+} oxides[18,27,43,48,50] (compare to Figure 5d).

Increasing the potential induces changes in the Ir 4f spectra. For semicrystalline IrO_x, the symmetric line shape observed at 0.25 V_{RHE} changes into an asymmetric shape during oxygen evolution at 1.65 V_{RHE}. The degree of Ir 4f asymmetry, quantified by integrating the Ir 4f difference spectrum, follows the potential dependence of the μ_1-O and μ_2-O peaks (see Figure 5e). This implies that the chemical state of Ir is affected by the oxidative deprotonation reactions 1−3. An obvious explanation is that Ir is oxidized in this process. Indeed, one may expect that Ir^{3+} will be oxidized to Ir^{4+}.

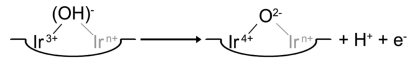

(4)

However, the deprotonation of all μ_2-OH sites alone would already require further oxidation of the material. Recent work suggests that this would lead to oxygen-centered oxidation.[11,18]

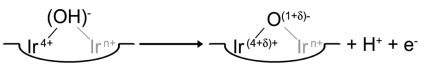

(5)

Hence, the changes in the Ir 4f spectrum may be caused by a combination of Ir-oxidation and modified Ir−O hybridization due to O-centered oxidation. This interpretation also holds for crystalline IrO_2, which shows a small increase in the Ir 4f asymmetry as well due to the oxidation of the surface. For amorphous IrO_x, we were unable to perform the analysis due to a lack of uniformity in the oxide thickness. However, in previous work on fully oxidized IrO_x nanoparticles, we showed that symmetry changes are even stronger for completely amorphous IrO_x than for the semicrystalline material.[10,27]

The data in Figures 4 and 5 make clear that similar deprotonation and oxidation phenomena occur on amorphous, semicrystalline, and crystalline iridium oxide. To investigate the similarities on a more quantitative level, we compared the potential dependence of the μ_2-O and μ_1-O signals, obtained from the O K-edge spectra in Figure 4. As shown in Figure 6, this analysis reveals similar deprotonation potentials for all Ir oxides. This indicates that not only the type of surface species formed at anodic potentials but also their energetics are fairly independent of the IrO_x crystal structure. This is further underpinned by the good agreement between the experimental data and MD simulations that we recently performed on the rutile IrO_2(110) surface,[26] which show that even a simple model system can capture the universal behavior of the Ir oxides rather well.

The S-curve observed in Figure 6a implies that the deprotonation of μ_2-OH to μ_2-O is completed under OER conditions. This is not the case for μ_1-OH deprotonation, which does not reach a plateau. This is particularly evident if one takes into account the ohmic drop for the data point at 1.85 V_{RHE} (real potential ~1.6 V_{RHE}). Incomplete μ_1-OH deprotonation is also implied by the ratio of the μ_1-O and μ_2-O signals in Figure 4, which is lower than that expected for

https://doi.org/10.1021/acscatal.1c05951
ACS Catal. 2022, 12, 5174−5184

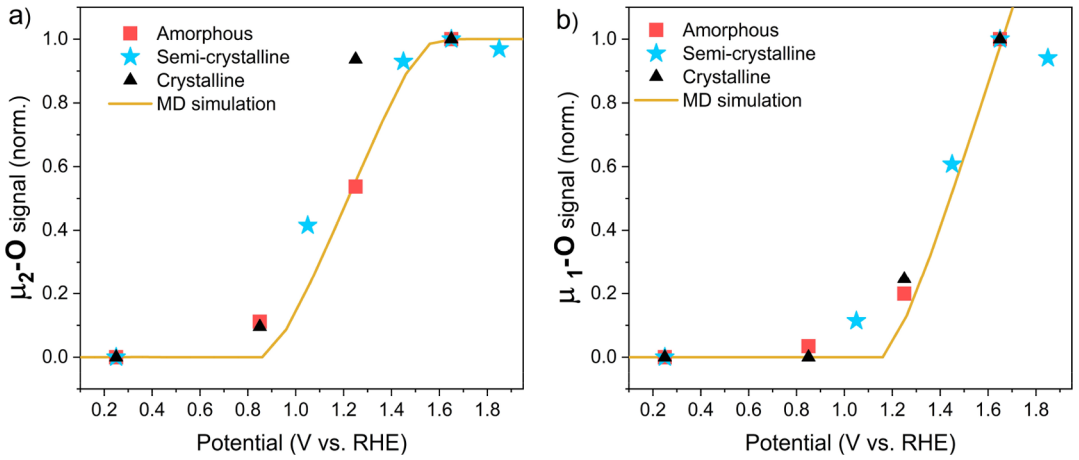

Figure 6. Potential dependence of the μ_2-O and μ_1-O signals from the data in Figure 4. (a) μ_2-O signal at 529 eV. (b) μ_1-O signal obtained from integration between 528 and 528.35 eV. The experimental μ_1-O and μ_2-O signals were background-subtracted using the spectra at 0.25 V_{RHE}, normalized to the μ_3-O intensity at 530 eV for the semicrystalline and crystalline samples, and finally normalized to one at 1.65 V_{RHE}. The solid lines show the theoretical coverage curves (also normalized at 1.65 V_{RHE}) extracted from MD simulations in ref 26.

complete deprotonation. If we consider the case of rutile IrO_2, we note that nearly all possible surface terminations have more μ_1-sites than μ_2-sites. Taking into account the relative resonance intensity for μ_1-O and μ_2-O species (8.8 vs 4.4, see Figure 4d), one would expect a μ_1-O/μ_2-O intensity ratio of at least 2, which is clearly not observed in the experiment. Overall, our analysis shows that μ_1-OH, μ_1-O, and μ_2-O are universally present on the oxides under OER conditions. In the case of semicrystalline and rutile oxides, the structure is completed by inert μ_3-O species.

So far, the analysis of our in situ spectroscopy data does not provide any explanation for the differences in activity and stability observed for the Ir oxides of varying crystallinity: we find that similar surface species are formed with similar formation energetics. However, Figures 4 and 5 show one notable difference between the samples: the magnitude of the deprotonation effects. Both the intensity of the μ_1-/μ_2-O signals and the change in Ir 4f symmetry increase for more amorphous materials, thus correlating with the activity and Ir dissolution rate.

To understand this correlation, one should understand where the trend in the deprotonation effects comes from. On a very general level, the explanation is straightforward: more amorphous oxides contain more undercoordinated oxygen atoms. In other words, they contain more μ_1- and μ_2-sites that can be (de)protonated and less inert μ_3-O. It appears that this increased number of μ_1- and μ_2-sites enhances both the OER and Ir dissolution rate. This can occur as a result of a higher number of active sites or due to a higher OER/dissolution rate per active site.

We will first analyze the possibility of an increased number of active sites. At first sight, this explanation seems plausible because μ_1-/μ_2-sites are universally involved in the OER mechanisms proposed in the literature.[8,51] Hence, our observation that there is a higher number of μ_1- and μ_2-sites in more amorphous oxides likely means that they contain a higher number of active sites. However, the trend in the OER and dissolution rate spans several orders of magnitude (see Figure 3 and Supporting Information Figures S10 and S11). If this were due solely to a variation in the number of active sites, then the number of active sites should also vary by several orders of magnitude. As shown in Figure 7, the variation in the μ_1-O and μ_2-O signals under OER conditions is much smaller.

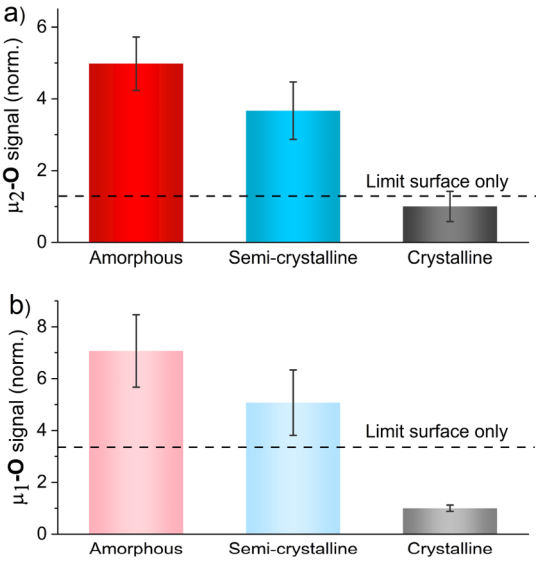

Figure 7. Comparison of the O K-edge signal from deprotonated species at 1.65 V_{RHE}. (a) μ_2-O signal at 529 eV. (b) μ_1-O signal obtained from integration between 528 and 528.35 eV. Both signals were obtained from spectra that were normalized to the overall edge jump at 550 eV. They are shown relative to the value found for crystalline IrO_2. The dashed lines indicate the signal intensity one could obtain from pure surface deprotonation with the highest μ_1-/μ_2-site density possible, relative to crystalline IrO_2 with a perfectly equilibrated surface. Details and assumptions of the analysis can be found in Supporting Information Sections S11 and S12.

Based on the analysis above, it seems unlikely that the trend in the OER and dissolution rate can be explained solely by the number of active sites. Hence, the OER and dissolution rate per active site must (also) be affected by the number of μ_1-/μ_2-sites in the electrode. In line with this, it was recently shown that the presence of μ_1-O and μ_2-O groups around the active sites promotes the OER on iridium oxide.[26] More specifically, deprotonating nearby μ_1-OH and μ_2-OH groups to μ_1-O/μ_2-O creates an electrophilic character in the active site, lowering the

https://doi.org/10.1021/acscatal.1c05951
ACS Catal. 2022, 12, 5174−5184

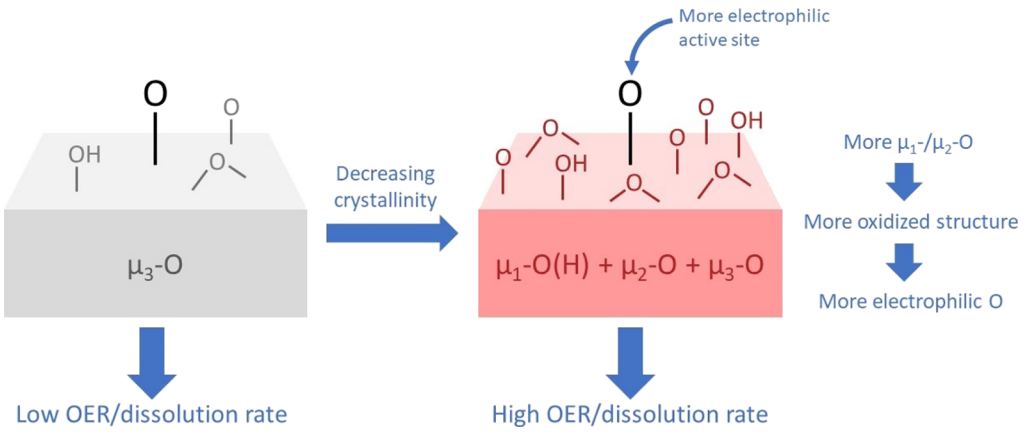

Figure 8. Schematic representation of the proposed *operando* structure−activity−stability relation.

barrier for the rate-limiting O−O coupling step. From our analysis here, it appears that having a higher density of μ_1-/μ_2-sites makes this activation effect stronger.

We can rationalize the promoting effect of a high density of μ_1-O/μ_2-O groups by considering the oxidation states in the material. In both crystalline and amorphous Ir oxides, Ir is octahedrally coordinated by O atoms. If all O atoms are μ_3-O groups, then each Ir atom formally has to compensate for a charge of $6 \times 1/3 \times -2 = -4$ from its surrounding O atoms. If we would replace the μ_3-O groups by μ_2-O groups, then the formal oxidation state of Ir would be $6 \times 1/2 \times 2 = 6$. As this example shows, introducing (deprotonated) μ_1-O/μ_2-O groups makes the material more oxidized. As discussed earlier, the oxidation will be centered not only on the Ir atoms but also on the oxygen atoms.[11,18,27] Hence, highly oxidized Ir oxides containing a high density of μ_1-O/μ_2-O groups will have a strong electrophilic character in the active μ_1-O sites, which ensures a low OER barrier[26] (as schematically depicted in Figure 8). Important to note is that any change in the OER barrier will have an exponential effect on the catalytic activity. Hence, even though the density of μ_1-O and μ_2-O groups only varies by factors of 7.1 and 5.0, respectively, this may cause orders-of-magnitude variation in the OER activity.

Since the promoting effect of the μ_1-O and μ_2-O groups around the active sites is purely electronic, both surface and subsurface μ_1-/μ_2-O groups can contribute to lowering the OER barrier. By analyzing the data in Figure 7, we can estimate the importance of the subsurface contribution. To this end, we consider the range of μ_1- and μ_2-site densities in all chemically reasonable IrO_2 surface structures. The μ_2-site density at the surface can only vary from 11.2 to 14.0 nm^{-2}, and for μ_1-sites, the density lies between 4.17 and 14.0 nm^{-2} (see Supporting Information section S12 for details). In other words, the surface μ_2-site density can only vary by a factor of 1.25 and the surface μ_1-site density by a factor of 3.35. This factor is indicated by the dashed lines in Figure 7. Comparing it to the much larger variations in the O K-edge signals, one can conclude that the majority of the μ_1-O and μ_2-O groups in semicrystalline and amorphous IrO_x are located in the subsurface region. Hence, under OER conditions, OH groups are deprotonated not only at the surface but also in the subsurface region. The catalyst oxidation that is associated with this may play a vital role in lowering the barrier for the OER.

Although the presence of μ_1-/μ_2-sites and their deprotonation under OER conditions favors high catalytic activity, they also appear to increase catalyst dissolution. We can rationalize this based on two factors. First, it is believed that the OER and steady-state Ir dissolution share one or more intermediates.[9,52] Hence, lowering the barrier for the OER can simultaneously lower the barrier for Ir dissolution. Similar to the case of the catalytic activity, the dissolution rate has an exponential dependence on the reaction barrier. In this way, the variation in μ_1-/μ_2-site density by a factor of 7.1/5.0 can cause observed orders-of-magnitude variation in the dissolution rate. A second factor affecting dissolution is that introducing μ_1-/μ_2-sites into the oxide lowers the connectivity in the lattice. As a result, fewer Ir−O bonds need to be broken per dissolution event. Thus, the oxygen coordination and protonation state of both surface and subsurface are vital for determining the kinetics of both oxygen evolution and catalyst dissolution under OER conditions.

CONCLUSIONS

By combining electrochemical characterization, Ir dissolution measurements, *operando* XAS, and XPS, we have shed light on the relation between the *operando* (OER) structure, activity and stability of iridium oxides ranging from amorphous to crystalline. Our work highlights the importance of oxide deprotonation reactions in determining the performance of the catalysts. Raising the potential into the OER regime universally results in μ_2-OH deprotonation and (limited) μ_1-OH deprotonation, with deprotonation potentials that are largely independent of the oxide's crystallinity. These deprotonation reactions oxidize the material, which is reflected in both the O and Ir atoms, as shown by *operando* O K-edge and Ir 4f spectra. Such oxidation creates an electrophilic character in the μ_1-O atoms on the surface, which makes them reactive for O−O coupling.[11,26,53] A key aspect we find here is that the deprotonation that activates the material for OER is not limited to the topmost surface layer but proceeds deeper into the material for semicrystalline and amorphous Ir oxides. Such subsurface deprotonation could lower the barrier for the OER through an electronic doping effect in the same way as recently established for surface deprotonation.[26] Thus, the subsurface deprotonation observed for amorphous and semicrystalline IrO_x can explain the high activity observed for these materials. However, the subsurface deprotonation might also lower the barrier for the dissolution of Ir species. Together with the lower oxygen connectivity that we found for less crystalline oxides, this could explain the correlation observed between crystallinity and stability. Thus, our results indicate that increasing the amount of μ_2-OH and μ_1-OH sites is a double-

https://doi.org/10.1021/acscatal.1c05951
ACS Catal. 2022, 12, 5174−5184

edged sword, with a positive impact on activity but a negative effect on stability. Our detailed insights into this effect provide handles for the tuning of iridium oxides for the oxygen evolution reaction and may serve as an inspiration for strategies to break the inverse correlation between activity and stability generally observed for the most active materials in the acid OER.

■ ASSOCIATED CONTENT

Supporting Information

The Supporting Information is available free of charge at https://pubs.acs.org/doi/10.1021/acscatal.1c05951.

Details on the sample preparation and characterization, cell configuration, analysis procedures, and additional experimental and theoretical data (PDF)

■ AUTHOR INFORMATION

Corresponding Author

Rik V. Mom − *Fritz Haber Institute of the Max Planck Society, 14195 Berlin, Germany; Leiden Institute of Chemistry, Leiden University, 2300 RA Leiden, The Netherlands;* orcid.org/0000-0002-5111-5591; Email: r.v.mom@lic.leidenuniv.nl

Authors

Lorenz J. Falling − *Fritz Haber Institute of the Max Planck Society, 14195 Berlin, Germany;* orcid.org/0000-0002-2622-5166

Olga Kasian − *Helmholtz-Zentrum Berlin GmbH, Helmholtz Institute Erlangen-Nürnberg, 14109 Berlin, Germany; Max Planck Institute for Iron Research, 40237 Düsseldorf, Germany;* orcid.org/0000-0001-6315-0637

Gerardo Algara-Siller − *Fritz Haber Institute of the Max Planck Society, 14195 Berlin, Germany*

Detre Teschner − *Fritz Haber Institute of the Max Planck Society, 14195 Berlin, Germany; Max Planck Institute for Chemical Energy Conversion, 45413 Mülheim an der Ruhr, Germany*

Robert H. Crabtree − *Department of Chemistry and Energy Sciences Institute, Yale University, New Haven, Connecticut 06520, United States;* orcid.org/0000-0002-6639-8707

Axel Knop-Gericke − *Fritz Haber Institute of the Max Planck Society, 14195 Berlin, Germany; Max Planck Institute for Chemical Energy Conversion, 45413 Mülheim an der Ruhr, Germany*

Karl J. J. Mayrhofer − *Helmholtz Institute Erlangen-Nürnberg for Renewable Energy (IEK-11), Forschungszentrum Jülich GmbH, 91058 Erlangen, Germany; Friedrich-Alexander-Universität Erlangen-Nürnberg, 91058 Erlangen, Germany;* orcid.org/0000-0002-4248-0431

Juan-Jesús Velasco-Vélez − *Fritz Haber Institute of the Max Planck Society, 14195 Berlin, Germany;* orcid.org/0000-0002-6595-0168

Travis E. Jones − *Fritz Haber Institute of the Max Planck Society, 14195 Berlin, Germany;* orcid.org/0000-0001-8921-7641

Complete contact information is available at: https://pubs.acs.org/10.1021/acscatal.1c05951

Notes

The authors declare no competing financial interest.

■ ACKNOWLEDGMENTS

This work was supported in part by the German Federal Ministry of Education and Research [BMBF project "Grundlagen elektrochemischer Phasengrenzen" (GEP), #13XP5023C]. The Helmholtz Zentrum Berlin (BESSY II synchrotron) is acknowledged for granting beam time. R.V.M. was financially supported through a Humboldt Research Fellowship by the Alexander von Humboldt Foundation. The authors thank Michael Hävecker and Eugen Stotz for their technical support.

■ REFERENCES

(1) van Troostwijk, A. P.; Deiman, J. R. Sur Une Manière de Decomposer l'Eau En Air Inflammable et En Air Vital. *Obs. Phys.* **1789**, *35*, 369.
(2) De Levie, R. The Electrolysis of Water. *J. Electroanal. Chem.* **1999**, *476*, 92−93.
(3) Anderson, D. L. Chemical Composition of the Mantle. *J. Geophys. Res.* **1983**, *88*, B41−B52.
(4) Danilovic, N.; Subbaraman, R.; Chang, K.-C.; Chang, S. H.; Kang, Y. J.; Snyder, J.; Paulikas, A. P.; Strmcnik, D.; Kim, Y.-T.; Myers, D.; Stamenkovic, V. R.; Markovic, N. M. Activity-Stability Trends for the Oxygen Evolution Reaction on Monometallic Oxides in Acidic Environments. *J. Phys. Chem. Lett.* **2014**, *5*, 2474−2478.
(5) Cherevko, S.; Geiger, S.; Kasian, O.; Kulyk, N.; Grote, J.-P.; Savan, A.; Shrestha, B. R.; Merzlikin, S.; Breitbach, B.; Ludwig, A.; Mayrhofer, K. J. J. Oxygen and hydrogen evolution reactions on Ru, RuO 2 , Ir, and IrO 2 thin film electrodes in acidic and alkaline electrolytes: A comparative study on activity and stability. *Catal. Today* **2016**, *262*, 170−180.
(6) Cherevko, S.; Zeradjanin, A. R.; Topalov, A. A.; Kulyk, N.; Katsounaros, I.; Mayrhofer, K. J. J. Dissolution of Noble Metals during Oxygen Evolution in Acidic Media. *ChemCatChem* **2014**, *6*, 2219−2223.
(7) Paoli, E. A.; Masini, F.; Frydendal, R.; Deiana, D.; Schlaup, C.; Malizia, M.; Hansen, T. W.; Horch, S.; Stephens, I. E. L.; Chorkendorff, I. Oxygen evolution on well-characterized mass-selected Ru and RuO2nanoparticles. *Chem. Sci.* **2015**, *6*, 190−196.
(8) Geiger, S.; Kasian, O.; Ledendecker, M.; Pizzutilo, E.; Mingers, A. M.; Fu, W. T.; Diaz-morales, O.; Li, Z.; Oellers, T.; Fruchter, L.; Ludwig, A.; Mayrhofer, K. J. J.; Koper, M. T. M.; Cherevko, S. The Stability Number as a Metric for Electrocatalyst Stability Benchmarking. *Nat. Catal.* **2018**, *1*, 508−515.
(9) Kasian, O.; Grote, J.-P.; Geiger, S.; Cherevko, S.; Mayrhofer, K. J. J. The Common Intermediates of Oxygen Evolution and Dissolution Reactions during Water Electrolysis on Iridium. *Angew. Chem., Int. Ed.* **2018**, *57*, 2488−2491.
(10) Frevel, L. J.; Mom, R.; Velasco-Vélez, J.-J.; Plodinec, M.; Knop-Gericke, A.; Schlögl, R.; Jones, T. E. In Situ X-ray Spectroscopy of the Electrochemical Development of Iridium Nanoparticles in Confined Electrolyte. *J. Phys. Chem. C* **2019**, *123*, 9146−9152.
(11) Pfeifer, V.; Jones, T. E.; Velasco Vélez, J. J.; Arrigo, R.; Piccinin, S.; Hävecker, M.; Knop-gericke, A.; Schlögl, R. In Situ Observation of Reactive Oxygen Species Forming on Oxygen-Evolving Iridium Surfaces. *Chem. Sci.* **2017**, *8*, 2143−2149.
(12) Mo, Y.; Stefan, I. C.; Cai, W.-B.; Dong, J.; Carey, P.; Scherson, D. A. In Situ Iridium LIII-Edge X-ray Absorption and Surface Enhanced Raman Spectroscopy of Electrodeposited Iridium Oxide Films in Aqueous Electrolytes. *J. Phys. Chem. B* **2002**, *106*, 3681−3686.
(13) Nong, H. N.; Reier, T.; Oh, H.-S.; Gliech, M.; Paciok, P.; Vu, T. H. T.; Teschner, D.; Heggen, M.; Petkov, V.; Schlögl, R.; Jones, T.; Strasser, P. A unique oxygen ligand environment facilitates water oxidation in hole-doped IrNiOx core-shell electrocatalysts. *Nat. Catal.* **2018**, *1*, 841−851.
(14) Merte, L. R.; Behafarid, F.; Miller, D. J.; Friebel, D.; Cho, S.; Mbuga, F.; Sokaras, D.; Alonso-Mori, R.; Weng, T.-C.; Nordlund, D.;

Nilsson, A.; Roldan Cuenya, B. Electrochemical Oxidation of Size-Selected Pt Nanoparticles Studied Using in Situ High-Energy-Resolution x-Ray Absorption Spectroscopy. *ACS Catal.* **2012**, *2*, 2371−2376.
(15) Pedersen, A. F.; Escudero-escribano, M.; Sebok, B.; Bodin, A.; Paoli, E.; Frydendal, R.; Friebel, D.; Stephens, I. E. L.; Rossmeisl, J.; Chorkendorff, I.; Nilsson, A. Operando XAS Study of the Surface Oxidation State on a Monolayer IrOx on RuOx and Ru Oxide Based Nanoparticles for Oxygen Evolution in Acidic Media. *J. Phys. Chem. B* **2018**, *122*, 878−887.
(16) Stefan, I. C.; Mo, Y.; Antonio, M. R.; Scherson, D. A. In Situ Ru LII and LIII Edge X-ray Absorption Near Edge Structure of Electrodeposited Ruthenium Dioxide Films. *J. Phys. Chem. B* **2002**, *106*, 12373−12375.
(17) Mom, R.; Frevel, L.; Velasco-Vélez, J.-J.; Plodinec, M.; Knop-gericke, A.; Schlögl, R. The Oxidation of Platinum under Wet Conditions Observed by Electrochemical X-ray Photoelectron Spectroscopy. *J. Am. Chem. Soc.* **2019**, *141*, 6537−6544.
(18) Velasco-Vélez, J. J.; Jones, T. E.; Streibel, V.; Hävecker, M.; Chuang, C.-H.; Frevel, L.; Plodinec, M.; Centeno, A.; Zurutuza, A.; Wang, R.; Arrigo, R.; Mom, R.; Hofmann, S.; Schlögl, R.; Knop-Gericke, A. Electrochemically Active Ir NPs on Graphene for OER in Acidic Aqueous Electrolyte Investigated by in Situ and Ex Situ Spectroscopies. *Surf. Sci.* **2019**, *681*, 1−8.
(19) Fierro, S.; Nagel, T.; Baltruschat, H.; Comninellis, C. Investigation of the Oxygen Evolution Reaction on Ti/IrO2 Electrodes Using Isotope Labelling and on-Line Mass Spectrometry. *Electrochem. Commun.* **2007**, *9*, 1969−1974.
(20) Stoerzinger, K. A.; Diaz-morales, O.; Kolb, M.; Rao, R. R.; Frydendal, R.; Qiao, L.; Wang, X. R.; Halck, N. B.; Rossmeisl, J.; Hansen, H. A.; Vegge, T.; Stephens, I. E. L.; Koper, M. T. M.; Shao-horn, Y. Orientation-Dependent Oxygen Evolution on RuO2 without Lattice Exchange. *ACS Energy Lett.* **2017**, *2*, 876−881.
(21) Diaz-Morales, O.; Calle-Vallejo, F.; de Munck, C.; Koper, M. T. M. Electrochemical Water Splitting by Gold: Evidence for an Oxide Decomposition Mechanism. *Chem. Sci.* **2013**, *4*, 2334−2343.
(22) Macounova, K.; Makarova, M.; Krtil, P. Oxygen evolution on nanocrystalline RuO2 and Ru0.9Ni0.1O2−δ electrodes - DEMS approach to reaction mechanism determination. *Electrochem. Commun.* **2009**, *11*, 1865−1868.
(23) Wohlfahrt-Mehrens, M.; Heitbaum, J. Oxygen Evolution on Ru and RuO2 Electrodes Studied Using Isotope Labelling and On-Line Mass Spectrometry. *J. Electroanal. Chem.* **1987**, *237*, 251−260.
(24) Zou, S.; Chan, H. Y. H.; Williams, C. T.; Weaver, M. J. Formation and Stability of Oxide Films on Platinum-Group Metals in Electrochemical and Related Environments As Probed by Surface-Enhanced Raman Spectroscopy: Dependence on the Chemical Oxidant. *Langmuir* **2000**, *16*, 754−763.
(25) Yeo, B. S.; Klaus, S. L.; Ross, P. N.; Mathies, R. A.; Bell, A. T. Identification of Hydroperoxy Species as Reaction Intermediates in the Electrochemical Evolution of Oxygen on Gold. *ChemPhysChem* **2010**, *11*, 1854−1857.
(26) Nong, H. N.; Falling, L. J.; Bergmann, A.; Klingenhof, M.; Tran, H. P.; Spöri, C.; Mom, R.; Timoshenko, J.; Zichittella, G.; Knop-Gericke, A.; Piccinin, S.; Pérez-Ramírez, J.; Cuenya, B. R.; Schlögl, R.; Strasser, P.; Teschner, D.; Jones, T. E. Key Role of Chemistry versus Bias in Electrocatalytic Oxygen Evolution. *Nature* **2020**, *587*, 408−413.
(27) Velasco-Vélez, J.-J.; Carbonio, E. A.; Chuang, C.-H.; Hsu, C.-J.; Lee, J.-F.; Arrigo, R.; Hävecker, M.; Wang, R.; Plodinec, M.; Wang, F. R.; Centeno, A.; Zurutuza, A.; Falling, L. J.; Mom, R. V.; Hofmann, S.; Schlögl, R.; Knop-Gericke, A.; Jones, T. E. Surface Electron-Hole Rich Species Active in the Electrocatalytic Water Oxidation. *J. Am. Chem. Soc.* **2021**, *143*, 12524−12534.
(28) Minguzzi, A.; Lugaresi, O.; Achilli, E.; Locatelli, C.; Vertova, A.; Ghigna, P.; Rondinini, S. Observing the Oxidation State Turnover in Heterogeneous Iridium-Based Water Oxidation Catalysts. *Chem. Sci.* **2014**, *5*, 3591−3597.
(29) Falling, L. J.; Mom, R. V.; Sandoval Diaz, L. E.; Nakhaie, S.; Stotz, E.; Ivanov, D.; Hävecker, M.; Lunkenbein, T.; Knop-Gericke, A.; Schlögl, R.; Velasco-Vélez, J.-J. Graphene-Capped Liquid Thin Films for Electrochemical Operando X-Ray Spectroscopy and Scanning Electron Microscopy. *ACS Appl. Mater. Interfaces* **2020**, *12*, 37680−37692.
(30) Klemm, S. O.; Topalov, A. A.; Laska, C. A.; Mayrhofer, K. J. J. Coupling of a High Throughput Microelectrochemical Cell with Online Multielemental Trace Analysis by ICP-MS. *Electrochem. Commun.* **2011**, *13*, 1533−1535.
(31) Saveleva, V. A.; Wang, L.; Teschner, D.; Jones, T.; Gago, A. S.; Friedrich, K. A.; Zafeiratos, S.; Schlögl, R.; Savinova, E. R. Operando Evidence for a Universal Oxygen Evolution Mechanism on Thermal and Electrochemical Iridium Oxides. *J. Phys. Chem. Lett.* **2018**, *9*, 3154−3160.
(32) Giannozzi, P.; Baroni, S.; Bonini, N.; Calandra, M.; Car, R.; Cavazzoni, C.; Ceresoli, D.; Chiarotti, G. L.; Cococcioni, M.; Dabo, I.; Dal Corso, A.; De Gironcoli, S.; Fabris, S.; Fratesi, G.; Gebauer, R.; Gerstmann, U.; Gougoussis, C.; Kokalj, A.; Lazzeri, M.; Martin-Samos, L.; Marzari, N.; Mauri, F.; Mazzarello, R.; Paolini, S.; Pasquarello, A.; Paulatto, L.; Sbraccia, C.; Scandolo, S.; Sclauzero, G.; Seitsonen, A. P.; Smogunov, A.; Umari, P.; Wentzcovitch, R. M. QUANTUM ESPRESSO: A Modular and Open-Source Software Project for Quantum Simulations of Materials. *J. Phys. Condens. Matter* **2009**, *21*, 395502.
(33) Perdew, J. P.; Burke, K.; Ernzerhof, M. Generalized Gradient Approximation Made Simple. *Phys. Rev. Lett.* **1996**, *77*, 3865−3868.
(34) Dal Corso, A. Pseudopotentials Periodic Table: From H to Pu. *Comput. Mater. Sci.* **2014**, *95*, 337−350.
(35) Marzari, N.; Vanderbilt, D.; De Vita, A.; Payne, M. C. Thermal Contraction and Disordering of the Al(110) Surface. *Phys. Rev. Lett.* **1999**, *82*, 3296−3299.
(36) Gougoussis, C.; Calandra, M.; Seitsonen, A. P.; Mauri, F. First-principles calculations of x-ray absorption in a scheme based on ultrasoft pseudopotentials: Fromα-quartz to high-Tccompounds. *Phys. Rev. B: Condens. Matter Mater. Phys.* **2009**, *80*, 075102.
(37) Taillefumier, M.; Cabaret, D.; Flank, A.-M.; Mauri, F. X-ray absorption near-edge structure calculations with the pseudopotentials: Application to theKedge in diamond andα-quartz. *Phys. Rev. B: Condens. Matter Mater. Phys.* **2002**, *66*, 195107.
(38) Pehlke, E.; Scheffler, M. Evidence for Site-Sensitive Screening of Core Holes at the Si and Ge (001) Surface. *Phys. Rev. Lett.* **1993**, *71*, 2338−2341.
(39) Buckley, D. N.; Burke, L. D. The oxygen electrode. Part 5.-Enhancement of charge capacity of an iridium surface in the anodic region. *J. Chem. Soc., Faraday Trans.* **1975**, *71*, 1447−1459.
(40) Johnson, B.; Ranjan, C.; Greiner, M.; Arrigo, R.; Schuster, M. E.; Höpfner, B.; Gorgoi, M.; Lauermann, I.; Willinger, M.; Knop-Gericke, A.; Schlögl, R. Characterization of Platinum and Iridium Oxyhydrate Surface Layers from Platinum and Iridium Foils. *ChemSusChem* **2016**, *9*, 1634−1646.
(41) Pavlovic, Z.; Ranjan, C.; Gao, Q.; Van Gastel, M.; Schlögl, R. Probing the Structure of a Water-Oxidizing Anodic Iridium Oxide Catalyst Using Raman Spectroscopy. *ACS Catal.* **2016**, *6*, 8098−8105.
(42) Carmo, M.; Fritz, D. L.; Mergel, J.; Stolten, D. A Comprehensive Review on PEM Water Electrolysis. *Int. J. Hydrogen Energy* **2013**, *38*, 4901−4934.
(43) Pfeifer, V.; Jones, T. E.; Velasco Vélez, J. J.; Massué, C.; Arrigo, R.; Teschner, D.; Girgsdies, F.; Scherzer, M.; Greiner, M. T.; Allan, J.; Hashagen, M.; Weinberg, G.; Piccinin, S.; Hävecker, M.; Knop-gericke, A.; Schlögl, R. The Electronic Structure of Iridium and Its Oxides. *Surf. Interface Anal.* **2016**, *48*, 261−273.
(44) Bergmann, A.; Martinez-Moreno, E.; Teschner, D.; Chernev, P.; Gliech, M.; de Araújo, J. F.; Reier, T.; Dau, H.; Strasser, P. Reversible Amorphization and the Catalytically Active State of Crystalline Co3O4 during Oxygen Evolution. *Nat. Commun.* **2015**, *6*, 8625.
(45) González-Flores, D.; Sánchez, I.; Zaharieva, I.; Klingan, K.; Heidkamp, J.; Chernev, P.; Menezes, P. W.; Driess, M.; Dau, H.;

https://doi.org/10.1021/acscatal.1c05951
ACS Catal. 2022, 12, 5174−5184

Montero, M. L. Heterogeneous Water Oxidation: Surface Activity versus Amorphization Activation in Cobalt Phosphate Catalysts. *Angew. Chem., Int. Ed.* **2015**, *54*, 2472−2476.
(46) Binninger, T.; Mohamed, R.; Waltar, K.; Fabbri, E.; Levecque, P.; Kötz, R.; Schmidt, T. J. Thermodynamic Explanation of the Universal Correlation between Oxygen Evolution Activity and Corrosion of Oxide Catalysts. *Sci. Rep.* **2015**, *5*, 12167.
(47) Wan, G.; Freeland, J. W.; Kloppenburg, J.; Petretto, G.; Nelson, J. N.; Kuo, D.-Y.; Sun, C.-J.; Wen, J.; Diulus, J. T.; Herman, G. S.; Dong, Y.; Kou, R.; Sun, J.; Chen, S.; Shen, K. M.; Schlom, D. G.; Rignanese, G.-M.; Hautier, G.; Fong, D. D.; Feng, Z.; Zhou, H.; Suntivich, J. Amorphization mechanism of SrIrO 3 electrocatalyst: How oxygen redox initiates ionic diffusion and structural reorganization. *Sci. Adv.* **2021**, *7*, No. eabc7323.
(48) Kahk, J. M.; Poll, C. G.; Oropeza, F. E.; Ablett, J. M.; Céolin, D.; Rueff, J.-P.; Agrestini, S.; Utsumi, Y.; Tsuei, K. D.; Liao, Y. F.; Borgatti, F.; Panaccione, G.; Regoutz, A.; Egdell, R. G.; Morgan, B. J.; Scanlon, D. O.; Payne, D. J. Understanding the Electronic Structure ofIrO2Using Hard-X-ray Photoelectron Spectroscopy and Density-Functional Theory. *Phys. Rev. Lett.* **2014**, *112*, 117601.
(49) Falling, L. Potential-Driven Surface Phase Transitions on Iridium (Hydr-)Oxides and Their Relation to Electrolytic Water Splitting. PhD Thesis, Fritz Haber Institute of the Max Planck Society, 2020.
(50) Freakley, S. J.; Ruiz-Esquius, J.; Morgan, D. J. The X-Ray Photoelectron Spectra of Ir, IrO2 and IrCl3 Revisited. *Surf. Interface Anal.* **2017**, *49*, 794−799.
(51) Shi, Z.; Wang, X.; Ge, J.; Liu, C.; Xing, W. Fundamental Understanding of the Acidic Oxygen Evolution Reaction: Mechanism Study and State-of-the-Art Catalysts. *Nanoscale* **2020**, *12*, 13249−13275.
(52) Kasian, O.; Geiger, S.; Li, T.; Grote, J.-P.; Schweinar, K.; Zhang, S.; Scheu, C.; Raabe, D.; Cherevko, S.; Gault, B.; Mayrhofer, K. J. J. Degradation of Iridium Oxides via Oxygen Evolution from the Lattice: Correlating Atomic Scale Structure with Reaction Mechanisms. *Energy Environ. Sci.* **2019**, *12*, 3548−3555.
(53) Pfeifer, V.; Jones, T. E.; Wrabetz, S.; Massué, C.; Velasco Vélez, J. J.; Arrigo, R.; Scherzer, M.; Piccinin, S.; Hävecker, M.; Knop-Gericke, A.; Schlögl, R. Reactive Oxygen Species in Iridium-Based OER Catalysts. *Chem. Sci.* **2016**, *7*, 6791−6795.

https://doi.org/10.1021/acscatal.1c05951
ACS Catal. 2022, 12, 5174−5184